A New Benchmark for Surface Radiation Products over the East Asia-Pacific Region Retrieved from the Himawari-8/AHI Next-Generation Geostationary Satellite

Husi Letu, Takashi Y. Nakajima, Tianxing Wang, Huazhe Shang, Run Ma, Kun Yang, Anthony J. Baran, Jerome Riedi, Hiroshi Ishimoto, Mayumi Yoshida, et al.

BAMS Article

A New Benchmark for Surface Radiation Products over the East Asia–Pacific Region Retrieved from the *Himawari-8*/AHI Next-Generation Geostationary Satellite

Husi Letu, Takashi Y. Nakajima, Tianxing Wang, Huazhe Shang, Run Ma, Kun Yang, Anthony J. Baran, Jerome Riedi, Hiroshi Ishimoto, Mayumi Yoshida, Chong Shi, Pradeep Khatri, Yihan Du, Liangfu Chen, and Jiancheng Shi

ABSTRACT: Surface downward radiation (SDR), including shortwave downward radiation (SWDR) and longwave downward radiation (LWDR), is of great importance to energy and climate studies. Considering the lack of reliable SDR data with a high spatiotemporal resolution in the East Asia–Pacific (EAP) region, we derived SWDR and LWDR at 10-min and 0.05° resolutions for this region from 2016 to 2020 based on the next-generation geostationary satellite *Himawari-8* (*H-8*). The SDR product is unique in terms of its all-sky features, high accuracy, and high-resolution levels. The cloud effect is fully considered in the SDR product, and the influence of high aerosol loadings and topography on the SWDR are considered. Compared to benchmark products of the radiation, such as Clouds and the Earth's Radiant Energy System (CERES) and the European Centre for Medium-Range Weather Forecasts (ECMWF) next-generation reanalysis (ERA5), and the Global Land Surface Satellite (GLASS), not only is the resolution of the new SDR product notably much higher, but the product accuracy is also higher than that of those products. In particular, hourly and daily root-mean-square errors of the new SWDR are 104.9 and 31.5 W m^{-2}, respectively, which are much smaller than those of CERES (at 121.6 and 38.6 W m^{-2}, respectively), ERA5 (at 176.6 and 39.5 W m^{-2}, respectively), and GLASS (daily of 36.5 W m^{-2}). Meanwhile, RMSEs of hourly and daily values of the new LWDR are 19.6 and 14.4 W m^{-2}, respectively, which are comparable to that of CERES and ERA5, and even better over high-altitude regions.

KEYWORDS: Algorithms; Cloud retrieval; Remote sensing

https://doi.org/10.1175/BAMS-D-20-0148.1

Corresponding authors: Husi Letu, husiletuw@hotmail.com; Jiancheng Shi, shijc@radi.ac.cn

In final form 15 October 2021

AFFILIATIONS: Letu—State Key Laboratory of Remote Sensing Science, Aerospace Information Research Institute, Chinese Academy of Sciences, Beijing, China, and Research and Information Center (TRIC), Tokai University, Kanagawa, Japan; **Nakajima**—Research and Information Center (TRIC), Tokai University, Kanagawa, Japan; **Wang and Du**—School of Geospatial Engineering and Science, Sun Yat-Sen University, Zhuhai, Guangdong, China; **Shang and Chen**—State Key Laboratory of Remote Sensing Science, Aerospace Information Research Institute, Chinese Academy of Sciences, Beijing, China; **Ma**—University of Chinese Academy of Sciences, Beijing, China; **Yang**—Department of Earth Science System, Tsinghua University, Beijing, China; **Baran**—Met Office, Exeter, and School of Physics, Astronomy and Mathematics, University of Hertfordshire, Hatfield, United Kingdom; **Riedi**—Laboratoire d'Optique Atmospheìrique, Sciences et Technologies, Université de Lille, Villeneuve d'Ascq, France; **Ishimoto**—Meteorological Research Institute, Japan Meteorological Agency, Tsukuba, Japan; **Yoshida**—Earth Observation Research Center, Japan Aerospace Exploration Agency, Tsukuba, Ibaraki, Japan; **C. Shi**—State Key Laboratory of Remote Sensing Science, Aerospace Information Research Institute, Chinese Academy of Sciences, Beijing, China, and Center for Global Environmental Research, National Institute for Environmental Studies, Tsukuba, Japan; **Khatri**—Center for Atmospheric and Oceanic Studies, Tohoku University, Sendai, Japan; **J. Shi**—National Space Science Center, Chinese Academy of Sciences, Beijing, China

Surface downward radiation (SDR), which includes shortwave downward radiation (SWDR) and longwave downward radiation (LWDR), is a fundamental component of the surface energy balance and one of the main factors influencing climate change, as well as the major forcing variable in many land surface and hydrological models (Pinker et al. 2005; Stephens et al. 2012; Wang and Dickinson 2013; Liang et al. 2019). Consequently, reliable SDR estimations are indispensable for Earth's energy cycle and climate studies as well as solar energy applications (Li et al. 1997; Yang et al. 2006; Ma and Pinker 2012).

Ground-based observations, numerical modeling, and satellite observations are all effective ways to estimate SDR (Liang et al. 2019). Ground-based observations are the most direct and reliable method to derive SDR data with a high precision and high temporal resolution (Huang et al. 2019); however, they do not exhibit a large spatial scale. In contrast, numerical modeling, which includes general circulation model (GCM) simulations and atmospheric reanalysis data, e.g., European Centre for Medium-Range Weather Forecasts (ECMWF) next-generation reanalysis (ERA5), provides spatiotemporally continuous SDR data at regional and global scales, but overall, its accuracy is limited, and the spatial resolution is relatively coarse for many applications (Decker et al. 2012). Based on high-performance numerical models and data assimilation techniques via combined ground and satellite measurements, the resolution and accuracy of recent reanalysis data have notably improved. For example, the spatial and temporal resolutions of ERA products have increased from 1° and 6 h, respectively, for the ERA-Interim product to 0.25° and 1 h, respectively, for the ERA5 product released in 2016, and the accuracy of ERA5 LWDR data are comparable to that of state-of-the-art satellite products (Hersbach et al. 2020; Tang et al. 2021). Remote sensing yields considerable advantages in surface radiation estimation with global/regional coverage and a high spatial resolution. Over the past decades, numerous SDR products based on low-Earth-orbit (LEO) and geosynchronous-equatorial-orbit (GEO) satellites have been released to accurately determine the energy budget at regional and global scales (Zhou and Cess 2001; Gupta 1989; Kato et al. 2011; Takenaka et al. 2011; Wang and Liang 2009). Most recently,

the cloud property and atmospheric radiation satellite products of Clouds and the Earth's Radiant Energy System (CERES) have been upgraded from edition 2 (Ed2) to edition 4 (Ed4). The CERES Ed4 product integrates LEO and GEO satellite data, and the spatiotemporal resolution (STR) of this product has been accordingly improved (Minnis et al. 2011), approaching that of traditional GEO satellites [e.g., Multifunctional Transport Satellite (MTSAT), Meteosat, and FengYun-2 series] at the global scale. The Global Land Surface Satellite (GLASS) product suite was released during the year 2000 to present. The daily SWDR products of the GLASS over land are at a spatial resolution of 0.05°, the generation of which is based on the lookup table (LUT) method by combining multiple geostationary and MODIS satellite data. The GLASS net radiation product (daytime) over land surfaces has been reported with an RMSE of 31.61 W m^{-2} (Liang et al. 2019, 2021).

Since 2010, next-generation geostationary satellites, such as the Geostationary Operational Environmental Satellite R-series (GOES-R), *Himawari-8* (*H-8*) (Bessho et al. 2016; Letu et al. 2019), and FengYun-4 (Yang et al. 2017), have been successfully launched, and their STR is notably higher than that of traditional GEO satellites and ERA5 and CERES products. Among them, *H-8* is the most widely studied by scientists worldwide since it provides multiple bands to retrieve accurate SDR data in the East Asia–Pacific (EAP) region (Letu et al. 2020). Unfortunately, to date, the uncertainties in the SDR products derived from *H-8* measurements caused by clouds, heavy aerosols, and topographic effects have not been comprehensively addressed. More importantly, its all-sky LWDR product has yet to be released.

Considering the lack of reliable SDR data with a high STR in the EAP region, we derive all-sky SWDR and LWDR data with unprecedented 10-min and 0.05° resolutions from 2016 to 2020 based on the new generation of geostationary measurements. More importantly, the new SDR product comprehensively considers the effects of the cloud phase, heavy aerosols, and topography on shortwave radiation, which have been neglected in many SDR studies.

Input data

H-8 *L1B data.* *H-8* is the next-generation geostationary satellite of the Japan Meteorological Agency (JMA), which was launched into geosynchronous orbit at approximately 140°E on 17 October 2014 and started its operation in 2015. The major instrument on board *H-8* is the Advanced Himawari Imager (AHI), which provides measurements in 16 separate channels, with central wavelengths ranging from 0.47 to 13.3 μm and spatial resolutions ranging from 0.5 to 2 km. The AHI scans the full disk (the whole Earth as observed from the satellite) at 10-min intervals. Additionally, the AHI scans four other areas (Japan, target, and two landmark areas) at a temporal resolution of 0.5 or 2.5 min to ensure a prompt response to meteorological conditions. The band data of the AHI are released in separate files, the radiance [W (m^2 sr μm)$^{-1}$] is recorded in all bands, the visible or near-infrared bands (bands 1–6) can be converted into the albedo or reflectance, and the infrared bands (bands 7–16) can be converted into the brightness temperature. The latest standard *H-8* L1B data are distributed in HSD and netCDF formats via www.eorc.jaxa.jp/ptree/index.html. The HSD format maintains the original resolution, while the netCDF format (60°S–60°N, 80°E–160°W) is reorganized to 0.05° with slightly lower coverage because of margin trimming.

H-8 *atmospheric products.* High-precision cloud microphysical parameters for different phases (ice and water clouds) are employed to derive the SDR product. Clouds are the most important factors influencing SDR (including both SWDR and LWDR). Cloud particles consisting of different thermodynamic phases impose different effects on SWDR. In recent years, we have developed official cloud products, including a cloud mask, cloud thermodynamic phase, optical thickness, and effective particle radius (examples are shown in

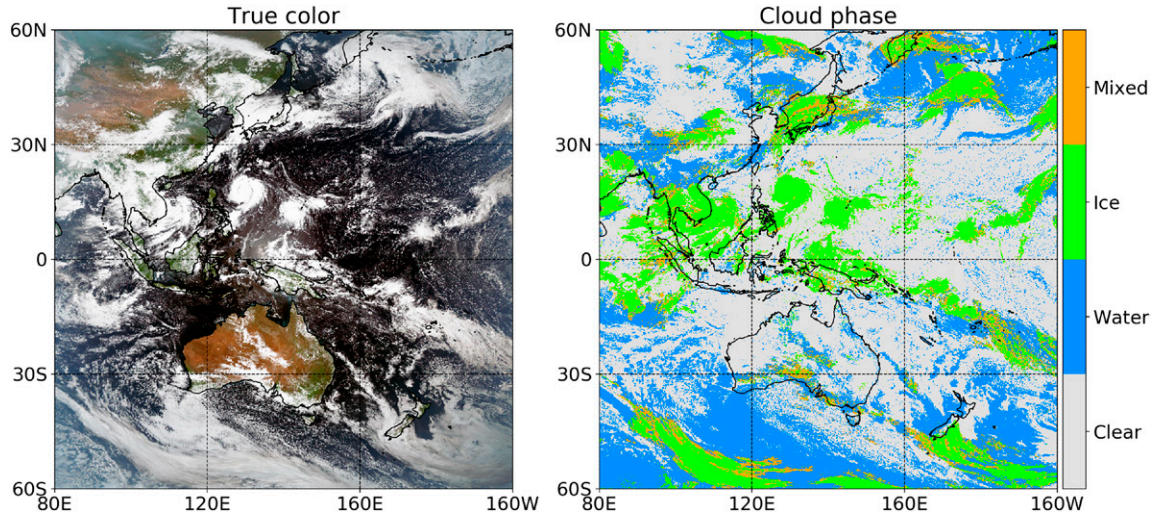

Fig. 1. (left) Full-disk true-color RGB image (0.64–0.51–0.46 μm) retrieved from the *H-8* AHI on 12 Sep 2016 (0300 UTC). (right) AHI cloud-phase results.

Figs. 1 and 2), for *H-8* satellite products (Letu et al. 2019, 2020). In this study, an SWDR retrieval algorithm is constructed based on the LUT method combined with radiative transfer principles. The macro- and microphysical parameters of different cloud phases are adopted as input parameters to calculate SWDR to improve its accuracy in regions covered by liquid or ice clouds.

The LWDR algorithm is an improved general regression method, trained mainly with CERES products and ground measurement data. It is a full-sky LWDR model based only on surface temperature (LST), column water vapor, and cloud-top temperature (CTT) (Wang et al. 2020). The advantage of this method is that it is easy to operate, and the required input data are readily available in both day- and nighttime, especially for the currently available moderate- and high-resolution satellite data. Most studies have reported that clouds severely modulate LWDR, and accurate derivation of longwave radiation under all-sky conditions remains a challenge in the community (Gupta et al. 2010; Kato et al. 2011). Moreover, almost all publicly available LWDR products exhibit a very coarse resolution (>0.25°) no matter space-based or reanalysis data, which cannot accurately reflect the variations in longwave radiation at regional and even global scales (Wang et al. 2018). Although the cloud-base temperature or height can directly relate to the cloudy thermal contribution (Zhou and Cess 2001), it is not easy to directly estimate from the satellites due to the opacity of the clouds in optical spectral range. In contrast, the CTT can be detected at both daytime and nighttime for most thermal infrared remote sensing missions, and many cloud-top height products are currently readily available for the public. Although the CTT cannot directly contribute to LWDR, a nonlinear positive correlation between the CTT and cloud-bottom temperature is found in our study. Thus, CTT is used as an indicator to quantify the cloud thermal contribution in a proper manner instead of using the temperature at cloud base. In this study, we quantified the cloud effect on LWDR via incorporation of the AHI CTT, and the all-sky LWDR at 0.05° and 10-min resolutions were then derived through further parameterization of the precipitable water vapor (PWV) and surface skin temperature (SKT). The CTT (Fig. 2) was retrieved from *H-8* data with a brightness temperature (10.8 μm)-based split-window algorithm according to reanalysis data and empirically determined thresholds (Nakajima et al. 2019).

Studies have indicated that high concentrations of aerosols (including dust or heavy haze) may strongly scatter or absorb solar radiation, resulting in a notable reduction in SWDR (Ma et al. 2020). In this study, aerosol optical thickness data that are more accurate in dusty or hazy

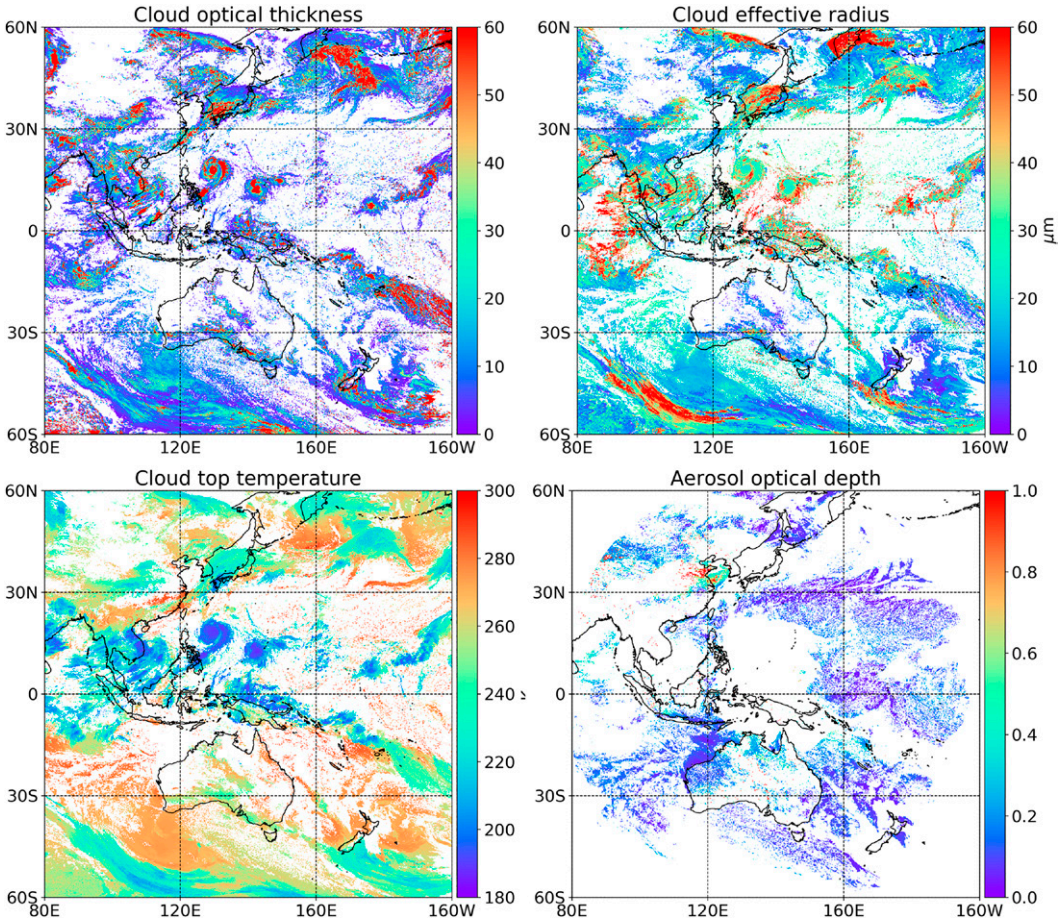

Fig. 2. Retrievals of (top left) cloud optical thickness, (top right) 2.3-μm cloud effective radius, (bottom left) cloud-top temperature, and (bottom right) aerosol optical thickness from the *H-8* AHI for the same time as that in Fig. 1.

areas are taken into account to improve the SWDR estimation accuracy, particularly under the high-aerosol loading conditions typical in East Asia. The aerosol optical depth (AOD) at 0.50 μm is inferred via a common aerosol retrieval algorithm of the JAXA-Ptree system (Mayumi et al. 2018), which considers different weights for the first five AHI channels based on the optimal estimation approach and is adopted as the input parameter of the algorithm to reduce the uncertainties in SWDR estimation. A comprehensive validation demonstrates that the *H-8*-derived AODs are generally consistent with those of AERONET with a root-mean-square error of 0.174 (Mayumi et al. 2018). An example of the AOD distribution in the EAP region is shown in Fig. 2.

Auxiliary data. The auxiliary data used to correct the SWDR estimation include PWV and ozone data at a spatial resolution of 0.25°, and surface pressure data at a spatial resolution of 0.1°. The auxiliary data used to correct the LWDR estimation include PWV and surface temperature data. All auxiliary data mentioned above are sourced from ERA5 data and resampled to 0.05° to collocate with the *H-8* measurements.

Validation data. The validation data we employed to quantitatively assess the accuracy of the SWDR obtained from 27 sites among 5 networks across the EAP region. In particular, there are 6 sites across Oceania maintained by the Australian Governments Bureau of Meteorology (BOM), 7 sites in coastal areas and the ocean of the Baseline Surface Radiation Network (BSRN) (Ohmura et al. 1998), 5 sites across the ocean of the Global Moored Buoy Array (GTMBA) (McPhaden et al. 2010), and 9 sites in mainland China affiliated with the

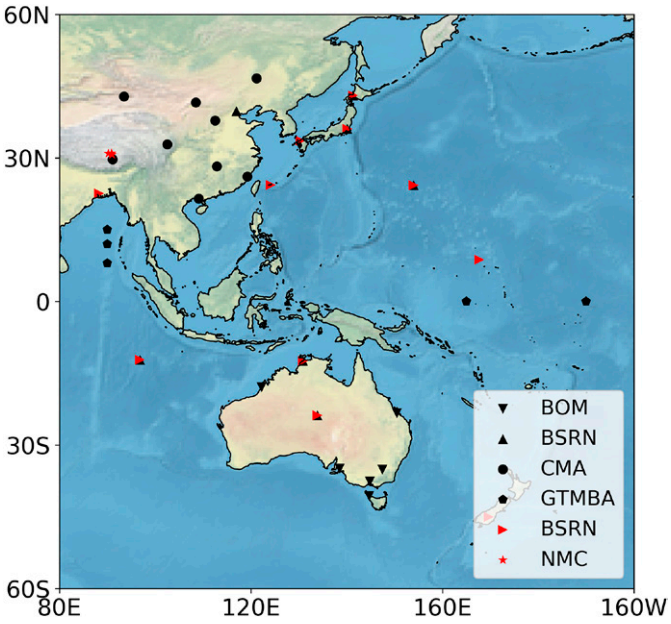

Fig. 3. Observational sites of SDR and their locations across the EAP region. The black and red markers indicate the sites of the SWDR and LWDR measurements used in this study. The sites of the different networks are marked with different shaped markers.

China Meteorological Administration (CMA). In addition, 11 sites from the BSRN and the other 3 sites from the Nam Co Watershed (NMC) are employed for the LWDR validation. Note that NMC is a ground observation network built by the Second Tibetan Plateau Scientific Expedition and Research Program (STEP) project, and the corresponding measurements include SWDR, LWDR, and net radiation. Moreover, the altitudes of these three stations are all above 4.5 km. The distributions of these observational sites are shown in Fig. 3, where the sites marked in black and red denote the SWDR and LWDR results, respectively, in this study. The stations at these sites conduct SDR measurements every 1–3 min except for those at the CMA sites.

Processing methodology

The algorithms yielding the all-sky SDR products are constructed according to the flowchart shown in Fig. 4. The input data include AHI L1 data containing geolocation information; AHI L2 products of the AOD; cloud optical thickness (COT), cloud effective radius (CER), and CTT for water and ice clouds; Moderate-Resolution Imaging Spectroradiometer (MODIS) L3 8-day (MCD43C3) surface albedo; and ERA5 SKT and PWV products.

We employ a precalculated LUT to combine aerosol (clear-sky) and cloud properties (cloudy-sky) combined with the viewing geometry (solar zenith angle, viewing zenith angle, and relative azimuth angle) to estimate SWDR (Letu et al. 2020). In addition, machine learning is adopted to accelerate SWDR searching in the very large LUT without reducing the accuracy (Ma et al. 2020). For simplicity, in the LUT calculation for SWDR retrieval, the surfaces are assumed to be homogeneous, and the PWV is assumed to be constant. A lack of surface elevation and actual PWV would lead to approximately 5% and 10% uncertainty in the estimation of SWDR (Zhang et al. 2019). Therefore, to reduce the uncertainties introduced by the above default assumptions on the surface elevation and PWV, normalized transmittance coefficients for both PWV and elevation are calculated. This is based on the near-real-time PWV, and the in situ elevation is adopted to further correct the estimated SWDR. The normalized transmittance coefficients are calculated according to Kim and Liang (2010) and Yang et al. (2006).

The LWDR derivation algorithm also consists of two parts, i.e., clear- and cloudy-sky conditions. Under clear-sky conditions, ERA5-derived SKT and PWV parameters are resampled to match the resolution of *H-8*. *H-8* cloud cover and CTT products are then incorporated to obtain the cloudy-sky LWDR. More details regarding the LWDR algorithm are provided in Wang et al. (2020). Note that a negative mean bias error (MBE) in the original LWDR algorithm over high-altitude conditions is corrected for in this study.

Features of the new products

In this section, four features of the new products are presented; they are characterized by high resolution, considering cloud effects, aerosol effects, and effects of complex terrain.

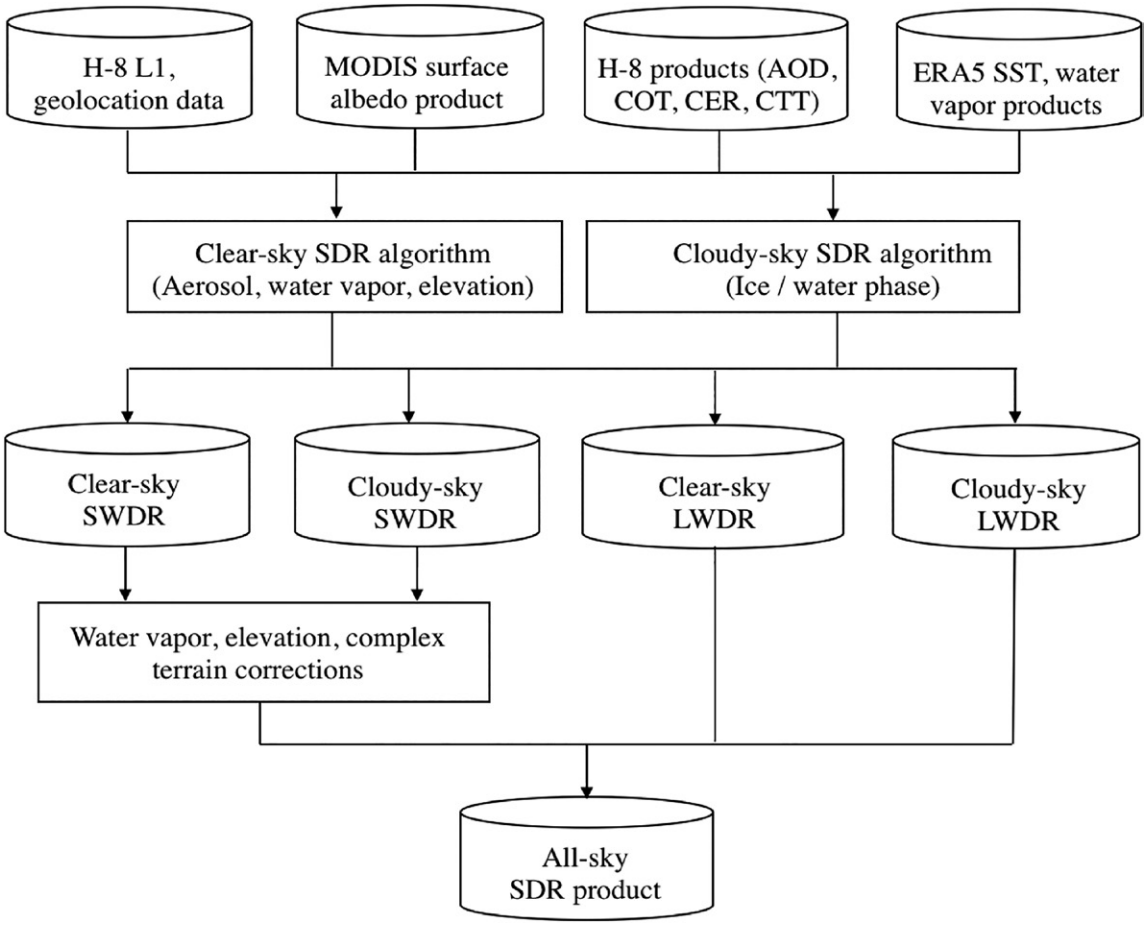

Fig. 4. Flowchart for the estimation of the all-sky SWDR and LWDR based on *H-8*.

The construction method of our products is developed based on the latest versions of the *H-8* aerosol and cloud retrieval algorithms, which minimize the propagation of uncertainties in aerosol or cloud retrieval to the estimation of SWDR and LWDR. The spatial details of *H-8* full-disk SDR products are evaluated with CERES and ERA5 results. Figures 5 and 6 show the daily mean SWDR and LWDR values on 1 January 2016 versus CERES and ERA5 values, in which areas a–c indicated in the top-left panels depict detailed regional SDR distributions of the above three mentioned products. Areas a–c are arbitrarily selected with relatively low, high, and intermediate SDR values, respectively. The high spatial resolution of the *H-8* SDR enables the zoomed results within areas a–c to be detailed. However, the ERA5 and CERES results are obviously pixelated.

As shown in Fig. 5, the high SWDR values along the belt at latitude 30°S and intermediate and low SWDR values at high northern latitudes for the three products exhibit similar spatial distributions. Based on the zoomed results within areas a–c, the *H-8* and CERES results are similar, while the ERA5 results exhibit inconsistent features in terms of the ranges of low SWDR values in areas a and c and high SWDR values in area b. The differences among these results in zoomed-in area b include a lower magnitude of the high SWDR values (300–400 W m^{-2}) estimated from *H-8* than that of the high SWDR values estimated from CERES and ERA5. In terms of the spatial resolution, the higher spatial resolution of the *H-8* products (0.05°) than that of the CERES (1.00°) and ERA5 (0.25°) products reveals more SWDR distribution details even in terms of the daily average values. The SWDR values estimated from *H-8* exhibit much more subtle changes, but both the CERES- and ERA5-estimated values are very homogeneous. The *H-8* product resolves the notable variation in SWDR that is not recognized by the other two data products.

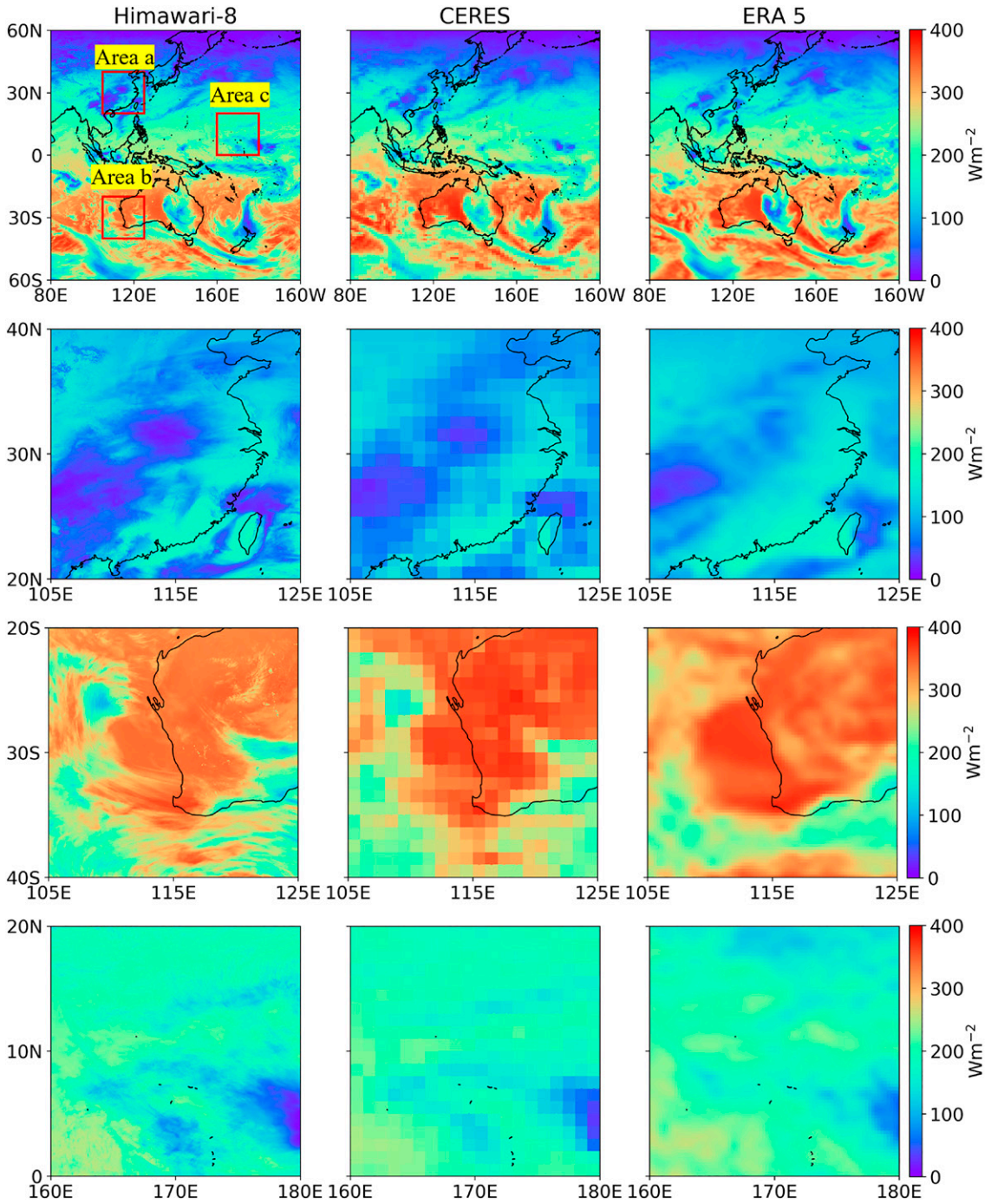

Fig. 5. Comparison of the daily mean (1 January 2016) SWDR values estimated from (left) *H-8*, (center) CERES, and (right) ERA5. (top) The full-disk SWDR and (second to fourth rows) show the SWDR values in zoomed-in areas a–c (their relative positions in the full disk are shown in the top-left panel).

In regard to the LWDR shown in Fig. 6, the high LWDR values are mainly distributed between the regions of 30°S and 30°N, which is in line with the spatial pattern of the temperature and PWV. Three enlarged regions (areas a–c) exhibit the differences among these three LWDR products. Generally, although the spatial pattern is very similar in the *H-8* full-disk region, more LWDR details are found in the *H-8* product, and other differences in terms of the LWDR magnitude among these products are also detected.

SWDR is a highly variable quantity that largely depends on the movement of the sun and atmospheric transmittance. Figure 7 shows an intercomparison of the diurnal variations in SWDR and LWDR from 21 to 25 August 2016, for the *H-8*, CERES, and ERA5 products, wherein the temporal

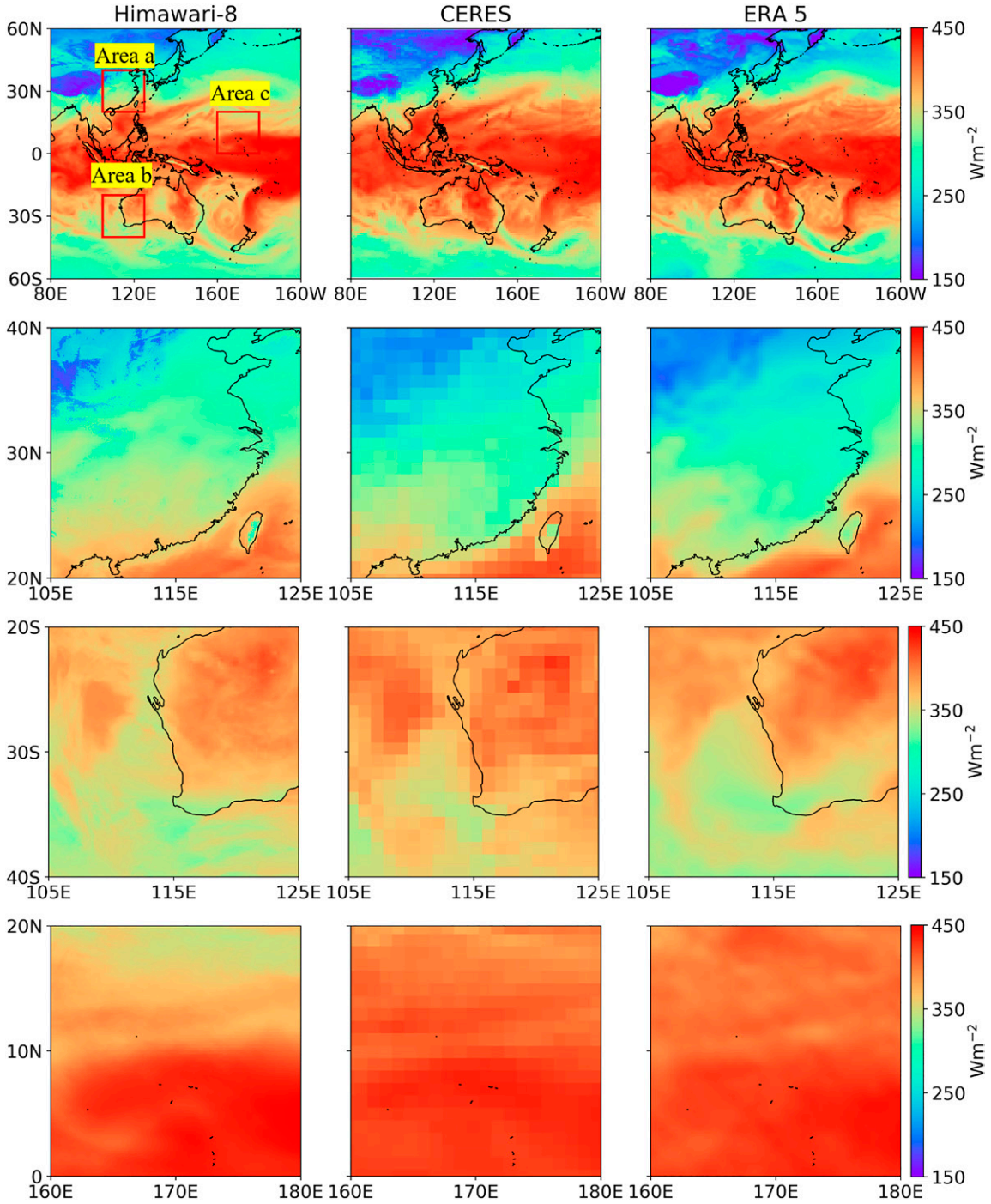

Fig. 6. Comparison of the daily mean LWDR values estimated from (left) *H-8*, (center) CERES, and (right) ERA5 for the same time as that in Fig. 5. (top) The the full-disk LWDR and (second to fourth rows) the LWDR values in zoomed-in areas a–c (their relative positions in the full disk are shown in the top-left panel).

resolution of CERES and ERA5 is 1 h, while the *H-8* product and ground-based measurements are shown at a temporal resolution of 10 min, of which the latter are adopted as a benchmark. Good agreement is observed among the four data products on both clear- and cloudy-sky days. However, from 21 to 25 August, when SWDR greatly varied, *H-8* clearly provided SWDR values closer to the ground measurements than either ERA5 or CERES did. Therefore, its high temporal resolution enables *H-8* to capture more variations in SWDR at competitive accuracy. Similar to SWDR, on the whole, the LWDR values obtained with *H-8*, CERES, and ERA5 reveal reasonable consistency with the in situ measurements. The diurnal variation in LWDR also attains high values during the daytime and low values during the nighttime, although the oscillation is not as notable as

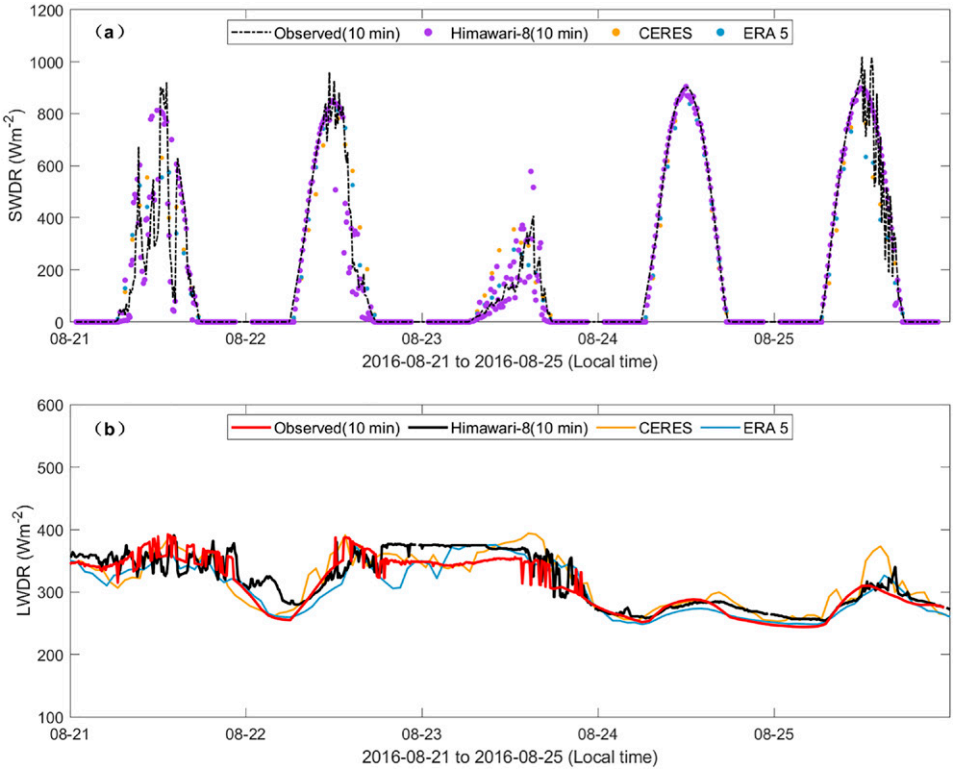

Fig. 7. Comparison of the diurnal variations in (a) SWDR and (b) LWDR among CERES (1 h), ERA5 (1 h), *H-8* (10 min), and ground-based measurements (10 min) from 21 to 25 Aug 2016. The zero-value dots during the nighttime denote invalid data.

that in SWDR. In addition, based on Fig. 7, we clearly observe the cloud effect on LWDR from 21 to 23 August 2016 (especially in regard to *H-8* and in situ LWDR), where the fluctuations in LWDR are consistent with the drastic variations in SWDR due to the presence of clouds, while this phenomenon is not captured in the CERES and ERA5 products due to their relatively coarse temporal resolution.

To investigate the influence of aerosols on the SWDR estimation, we validated the *H-8*-derived SWDR product against ground-based measurements at the Xianghe site (39.78°N, 116.98°E), which is an AERONET site located in North China with a high probability of air pollution in the winter. The corresponding SWDR products retrieved from CERES and ERA5 are also compared. Figure 8 (left) shows that the *H-8*-derived hourly SWDR exhibits a higher consistency with the in situ measurements under low-aerosol loading condition. In the polluted case shown in Fig. 8 (right), the variation in the hourly *H-8*-derived SWDR values approximately coincides with that in the ground observations from 1000 to 1400 local time, while the CERES and ERA5 SWDR values are over- and underestimated, respectively. Owing to the comprehensive modeling of the aerosol effects on solar radiative transfer, the current algorithm based on *H-8* yields a generally more accurate estimation of the hourly SWDR. In contrast, the corresponding CERES and ERA5 products exhibit large discrepancies when a high aerosol contamination level occurs, from approximately 1000 to 1400 local time.

Another characteristic of our SWDR products is that the influence of a complex topography is considered for the Tibetan Plateau region. Current surface radiation products ignore the influence of topographic variability on the derived radiation by simply assuming that the surface is horizontal and uniform, resulting in unreliable estimations in rugged regions. However, to date, few models are available operationally that consider this effect at large scales. Based on the topographically corrected shortwave radiation model proposed by Wang et al. (2018), a case SWDR product for the Tibetan Plateau (22°–45°N, 80°–112°E) was developed

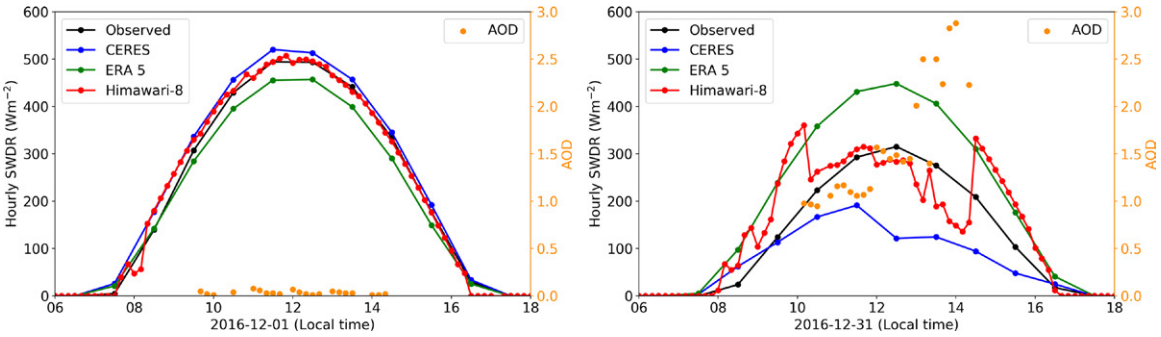

Fig. 8. Comparison of the hourly variations in SWDR among CERES, ERA5, *H-8*, and ground-based measurements (Xianghe, China) under (left) clean and (right) polluted conditions. The AOD retrieved from the *H-8* AHI is shown on the right-hand *y* axis.

via incorporation of the *H-8* SWDR product mentioned above. As a randomly selected datum, the impact of terrain correction on SWDR in a small subregion of the Tibetan Plateau under relatively clear-sky conditions is illustrated in Fig. 9. Before topographic correction, the SWDR values are very homogeneous with unrecognizable ground surface features, and the vast majority of the selected areas exhibits a rather fixed value (approximately 760 W m^{-2}). In contrast, the corrected SWDR values reveal subtle variations, especially on shady and sunny slopes, and the difference between the maximum and minimum SWDR values in the corrected radiation map is approximately 700 W m^{-2}, indicating very high spatial dynamics in the SWDR values.

Validation of the new products

To quantitatively verify the performance of new SWDR products, we selected three well-known SWDR products, the CERES, ERA5 and GLASS products to compare. Their spatial resolutions vary from 0.05° to 1°. All the SWDR products are compared with ground-based measurements in the EAP region (see Fig. 3) through scatter diagrams, as shown in Figs. 10 and 11. Since the GLASS SWDR product is provided on a daily scale, validation with GLASS is only conducted at a daily scale. It is known that the validation of shortwave radiation products against ground measurements can be influenced by the spatial resolution that has been adopted. So, all products are aggregated to the same spatial resolution (1°) for the validation. The accuracy is evaluated via the root-mean-square error (RMSE), MBE, and correlation coefficient (*R*).

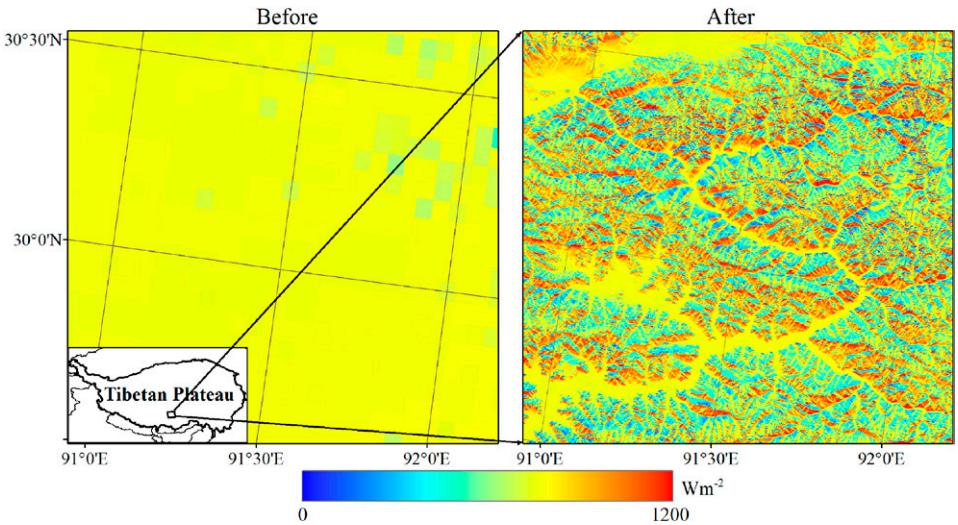

Fig. 9. SWDR estimations based on the *H-8* AHI over the Tibetan Plateau on 10 Jan 2018 (0600 UTC): (left) before terrain correction and (right) after terrain correction.

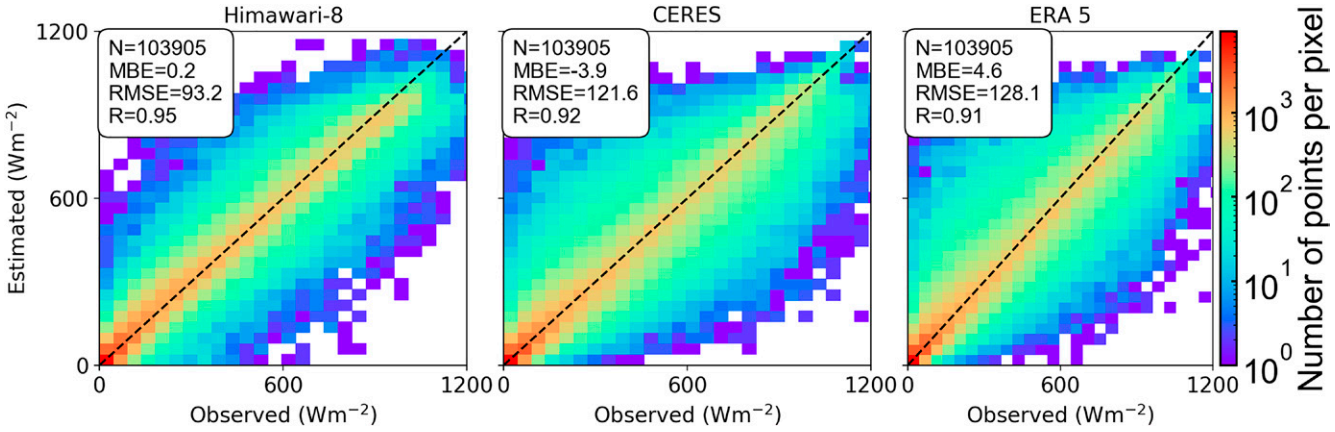

Fig. 10. Comparison of the hourly SWDR results of (left) *H-8*, (center) CERES, and (right) ERA5 to ground-based measurements in 2016. MBE and RMSE are expressed in W m^{-2}. The number of ground sites is 27.

Validation of hourly SWDR values retrieved from *H-8*, CERES, and ERA5 against the ground observations indicates that the RMSE values are 104.9, 121.6, and 176.6 W m^{-2}, respectively; the MBE values are 3.3, –3.9, and 7.0 W m^{-2}; respectively, and the *R* values are 0.94, 0.92, and 0.82, respectively (Fig. 10). Validation of the daily SWDR values retrieved from *H-8*, CERES, and ERA5 against the ground observations shows that the RMSE values are 31.5, 38.6, and 39.5 W m^{-2}, respectively. The MBE values were found to be 1.4, –2.0, and 1.3 W m^{-2}, respectively, and the *R* values are 0.95, 0.92, and 0.91, respectively (Fig. 11).

Notably, the abovementioned SWDR validation is done with measurements from 27 sites (Fig. 3), and the comparison with GLASS below is done with 19 land sites because the GLASS SWDR product does not provide data over ocean areas. As summarized in Table 1, the SWDR validation under the same spatial resolution shows that the RMSE values for *H-8*, CERES, ERA5, and GLASS are 30.8, 39.6, 39.3, and 36.5 W m^{-2}, respectively. In conclusion, the comparison at both the daily and hourly scales reveals that the *H-8*-derived SWDR results attain the best performance.

Similarly, ground-based measurements collected at the 11 sites shown in Fig. 3 (red marks) are adopted to validate the L-WDR results (Figs. 12 and 13). To ensure that these three products are theoretically comparable, the *H-8* and ERA5 products are aggregated to the coarser spatial resolution of CERES (1° × 1°). It can be readily concluded that the CERES-, ERA5-, and *H-8*-derived LWDR values exhibit comparable accuracy at both the hourly and daily scales. Validation of the hourly LWDR derived from *H-8*, CERES, and ERA5 against the ground measurements reveals that the RMSE values are 19.6, 20.5, and 17.2 W m^{-2},

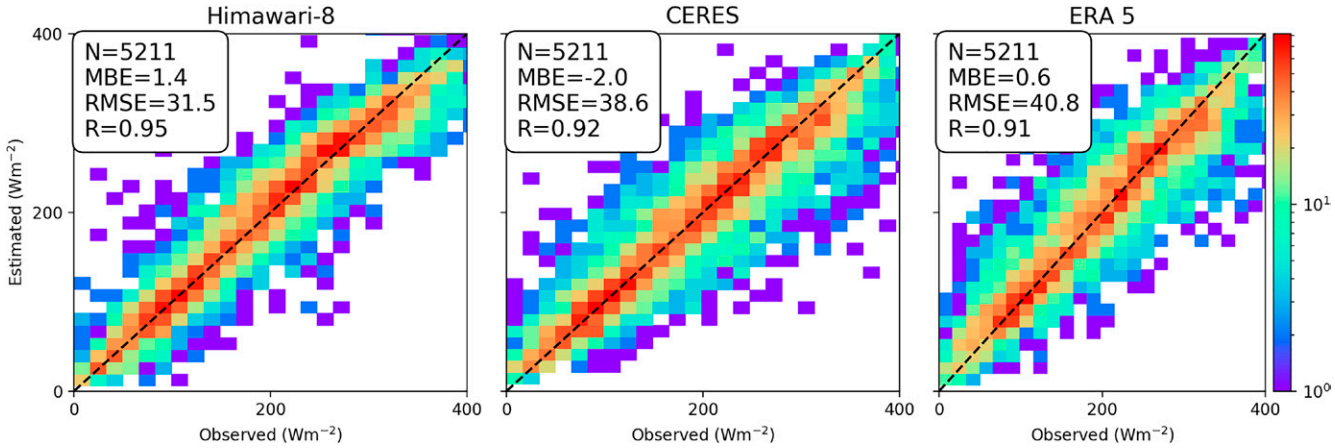

Fig. 11. As in Fig. 10, but for the daily SWDR results.

Table 1. Summary of SWDR validation results (note that the GLASS only has SWDR over land).

	Himawari-8	CERES	ERA5	GLASS	Sites
Hourly					
MBE (W m^{-2})	3.3	−3.9	7.0	—	19 land sites + 8 ocean sites
RMSE (W m^{-2})	104.9	121.6	176.6	—	
R	0.94	0.92	0.82	—	
Daily					
MBE (W m^{-2})	1.4	−2.0	1.3	—	19 land sites + 8 ocean sites
RMSE (W m^{-2})	31.5	38.6	39.5	—	
R	0.95	0.92	0.91	—	
Daily					
MBE (W m^{-2})	0	−4.6	−0.6	−11.7	19 land sites
RMSE (W m^{-2})	30.8	39.6	39.3	36.5	
R	0.96	0.93	0.93	0.94	

respectively. The MBE values are −1.8, 2.7, and −5.7 W m^{-2}, respectively, and the *R* values are 0.95, 0.94, and 0.97, respectively (Fig. 12). The corresponding validation of the daily *H-8*, CERES, and ERA5 results indicates that the RMSE values are 14.4, 13.8, and 11.0 W m^{-2}, respectively. The MBE values are −1.9, 2.6, and −5.8 W m^{-2}, and the *R* values are 0.97, 0.97, and 0.99, respectively (Fig. 13). Relatively speaking, ERA5 has the highest accuracy but with the largest MBE values in the EAP region, and *H-8* attains a very similar performance to that of CERES. Except for the accuracy, the *H-8* LWDR has higher spatiotemporal resolutions (10 min, 0.05°) than CERES and ERA5. Notably, the *H-8* LWDR product is slightly overestimated compared to the ground-based observations when the observed LWDR is relatively low (200–250 W m^{-2}) (Fig. 12). Many existing studies in the literature proved that LWDR is very sensitive to water vapor (Gupta 1989; Zhou and Cess 2001; Kato et al. 2011; Wang et al. 2018), especially for the cases with lower water vapor loading, and we have found similar problems with our method; fortunately, this is not too serious.

However, it has been reported that ERA5 is comparable to or outperforms current satellite LWDR products at coarser scales (Tang et al. 2021), to some extent. Our study reveals that ERA5 demonstrates a poor accuracy over some regions, especially over high-altitude areas. Specifically, we verified the hourly radiation of the three products versus ground measurements from 1 to 15 December 2019 at the NMC site (Fig. 3) over the Tibetan Plateau. The RMSE values of *H-8*, CERES and ERA5 LWDR are 18.1, 20.6, and 31.9 W m^{-2}, respectively, the MBE values are −5.5, −6.3, and −23.3 W m^{-2}, respectively; and the *R* values are 0.96,

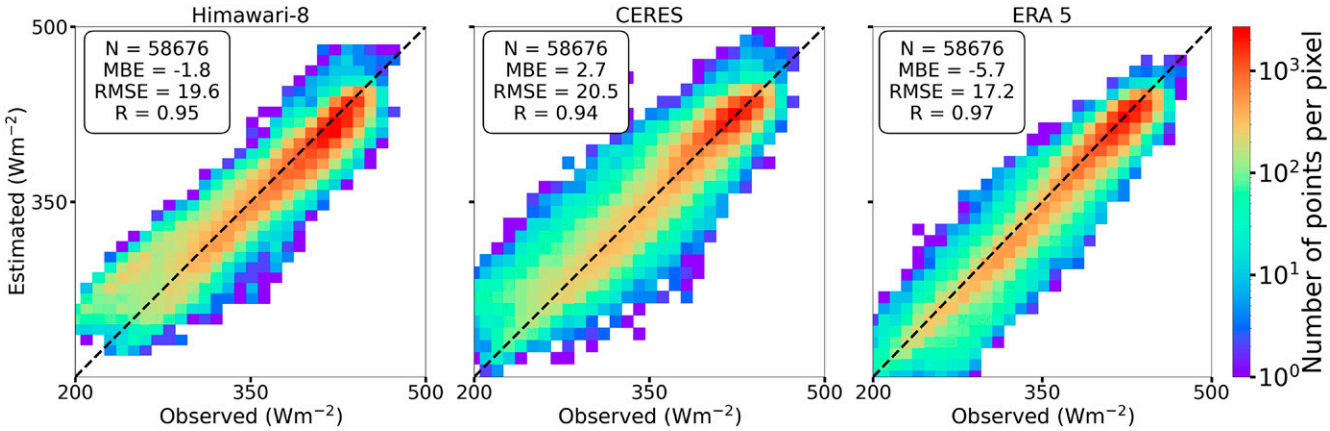

Fig. 12. Comparison of the hourly LWDR results of (left) *H-8*, (center) CERES, and (right) ERA5 to ground-based measurements in 2016. MBE and RMSE are expressed in W m^{-2}. The number of ground sites is 7.

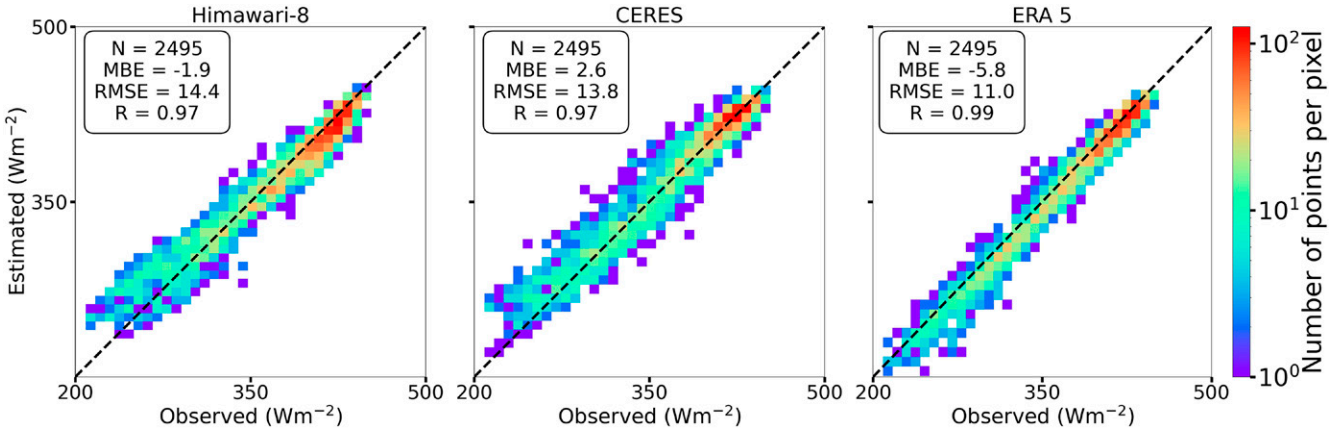

Fig. 13. As in Fig. 12, but for the daily LWDR results.

0.95, and 0.95, respectively. It is shown that the *H-8* product has the best accuracy in both MBE and RMSE, while ERA5 has the worst accuracy in high-altitude regions. In particular, this dataset has a notably low bias in winter in the Tibetan Plateau region. Figure 14 demonstrates the hourly variations in LWDR over NMC sites over the Tibetan Plateau from 1 to 15 December 2019. This result shows that the *H-8* LWDR is very similar to that of CERES; however, the large magnitude of MBE in the ERA5 LWDR can be clearly detected.

Summary

Surface downward radiation (SDR), including shortwave downward radiation (SWDR) and longwave downward radiation (LWDR), is a fundamental component of the energy budget of the Earth–atmosphere system. The Advanced Himawari Imager (AHI) on board the *Himawari-8* (*H-8*) satellite, as a new-generation geostationary satellite, receives high spatial and high temporal resolution spectral signals, which provides a unique opportunity to accurately estimate SDR in the East Asia–Pacific (EAP) region.

In this study, we developed an all-sky SDR product with high spatial (0.05°) and temporal (10 min) resolutions from 2016 to 2020 in the EAP region based on AHI data. The advantages of the new SDR product are as follows:

1) The SDR product is unique in its high spatiotemporal resolution and improved overall accuracy. The spatial resolution and accuracy of the new SWDR product is significantly higher than that of the Earth's Radiant Energy System (CERES) and the European Centre for Medium-Range Weather Forecasts (ECMWF) next-generation reanalysis (ERA5).

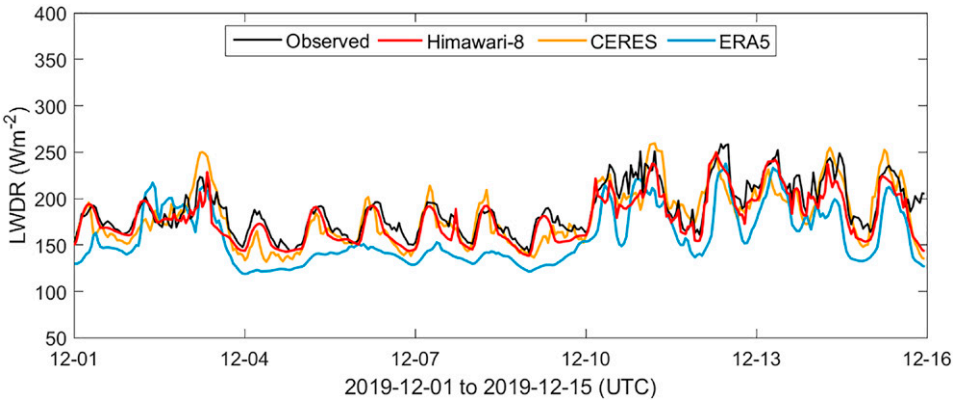

Fig. 14. Hourly variations of *H-8*, CERES, and ERA5 LWDR products from 1 to 15 Dec 2019 at NMC sites over the Tibetan Plateau.

The new SWDR is at the same spatial resolution as the SWDR of the Global Land Surface Satellite (GLASS) product, but the former has higher temporal resolution and accuracy than the latter.

2) In the calculation of shortwave radiation, in addition to atmospheric gases and altitude, cloud phases, heavy haze, and complex terrain conditions are fully considered.
3) In the derivation of longwave radiation, a generalized parameterization scheme is employed via incorporation of the cloud-top temperature, total column water vapor, and surface skin temperature.

The root-mean-square error (RMSE) of the hourly and daily average shortwave SDR estimation is notably smaller than those of CERES and ERA5, and the RMSE of the longwave SDR results is at least comparable to that of the CERES and ERA5 products (smaller than 15 W m^{-2} at a daily scale). Particularly, over high-altitude regions, the new *H-8* product is obviously superior to the ERA5 and CERES products in terms of both accuracy and spatiotemporal resolution. The developed SDR products, including SWDR and LWDR, will be available via the National Tibetan Plateau Data Center (http://data.tpdc.ac.cn/zh-hans/about/) upon manuscript acceptance.

In summary, compared to previous products, the new products developed in this study exhibit outstanding characteristics and high accuracy. The high-accuracy and high-resolution products may be useful for radiation budget studies and driving land models as well as the reference of solar energy.

Acknowledgments. This work was supplied by National Key R&D Program of China 2018YFA0605401; National Natural Science Foundation of China 42025504, 42022008, and 41771395; and Second Tibetan Plateau Scientific Expedition and Research Program (STEP) 2019QZKK0206.

References

Bessho, K., K. Date, M. Hayashi, A. Ikeda, and R. Yoshida, 2016: An introduction to Himawari-8/9—Japan's new-generation geostationary meteorological satellites. *J. Meteor. Soc. Japan*, **94**, 151–183, https://doi.org/10.2151/jmsj.2016-009.

Decker, M., M. A. Brunke, Z. Wang, K. Sakaguchi, X. Zeng, and M. G. Bosilovich, 2012: Evaluation of the reanalysis products from GSFC, NCEP, and ECMWF using flux tower observations. *J. Climate*, **25**, 1916–1944, https://doi.org/10.1175/JCLI-D-11-00004.1.

Gupta, S. K., 1989: A parameterization for longwave surface radiation from sun-synchronous satellite data. *J. Climate*, **2**, 305–320, https://doi.org/10.1175/1520-0442(1989)002%3C0305:APFLSR%3E2.0.CO;2.

——, D. P. Kratz, P. W. Stackhouse, A. C. Wilber, T. Zhang, and V. E. Sothcott, 2010: Improvement of surface longwave flux algorithms used in CERES processing. *J. Appl. Meteor. Climatol.*, **49**, 1579–1589, https://doi.org/10.1175/2010JAMC2463.1.

Hersbach, H., and Coauthors, 2020: The ERA5 global reanalysis. *Quart. J. Roy. Meteor. Soc.*, **146**, 1999–2049, https://doi.org/10.1002/qj.3803.

Huang, G., Z. Li, X. Li, S. Liang, and Y. Zhang, 2019: Estimating surface solar irradiance from satellites: Past, present, and future perspectives. *Remote Sens. Environ.*, **233**, 111371, https://doi.org/10.1016/j.rse.2019.111371.

Kim, H.-Y., and S. Liang, 2010: Development of a hybrid method for estimating land surface shortwave net radiation from MODIS data. *Remote Sens. Environ.*, **114**, 2393–2402, https://doi.org/10.1016/j.rse.2010.05.012.

Kato, S., and Coauthors, 2011: Improvements of top-of-atmosphere and surface irradiance computations with CALIPSO-, CloudSat-, and MODIS-derived cloud and aerosol properties. *J. Geophys. Res.*, **116**, D19209, https://doi.org/10.1029/2011JD016050.

Letu, H., and Coauthors, 2019: Ice cloud properties from Himawari-8/AHI next-generation geostationary satellite: Capability of the AHI to monitor the DC cloud generation process. *IEEE Trans. Geosci. Remote Sens.*, **57**, 3229–3239, https://doi.org/10.1109/TGRS.2018.2882803.

——, and Coauthors, 2020: High-resolution retrieval of cloud microphysical properties and surface solar radiation using Himawari-8/AHI next-generation geostationary satellite. *Remote Sens. Environ.*, **239**, 111583, https://doi.org/10.1016/j.rse.2019.111583.

Li, Z., L. Moreau, and A. Arking, 1997: On solar energy disposition: A perspective from observation and modeling. *Bull. Amer. Meteor. Soc.*, **78**, 53–70, https://doi.org/10.1175/1520-0477(1997)078<0053:OSEDAP>2.0.CO;2.

Liang, S., D. Wang, T. He, and Y. Yu, 2019: Remote sensing of Earth's energy budget: Synthesis and review. *Int. J. Digit. Earth*, **12**, 737–780, https://doi.org/10.1080/17538947.2019.1597189.

Liang S., and Coauthors, 2021: The Global Land Surface Satellite (GLASS) product suite. *Bull. Amer. Meteor. Soc.*, **102**, E323–E337, https://doi.org/10.1175/BAMS-D-18-0341.1.

Ma, R., H. Letu, K. Yang, T. Wang, and L. Chen, 2020: Estimation of surface shortwave radiation from Himawari-8 satellite data based on a combination of radiative transfer and deep neural network. *IEEE Trans. Geosci. Remote Sens.*, **58**, 5304–5316, https://doi.org/10.1109/TGRS.2019.2963262.

Ma, Y., and R. T. Pinker, 2012: Modeling shortwave radiative fluxes from satellites. *J. Geophys. Res.*, **117**, D23202, https://doi.org/10.1029/2012JD018332.

McPhaden, M. J., and Coauthors, 2010: The global tropical moored buoy array. *Proceedings OceanObs'09: Sustained Ocean Observations and Information for Society, ESA Publ. WPP-306*, 15 pp., https://doi.org/10.5270/OceanObs09.cwp.61.

Minnis, P., and Coauthors, 2011: CERES Edition-2 cloud property retrievals using TRMM VIRS and Terra and Aqua MODIS data—Part I: Algorithms. *IEEE Trans. Geosci. Remote Sens.*, **49**, 4374–4400, https://doi.org/10.1109/TGRS.2011.2144601.

Nakajima, T. Y., and Coauthors, 2019: Theoretical basis of the algorithms and early phase results of the GCOM-C (Shikisai) SGLI cloud products. *Prog. Earth Planet. Sci.*, **6**, 52, https://doi.org/10.1186/s40645-019-0295-9.

Ohmura, A., and Coauthors, 1998: Baseline Surface Radiation Network (BSRN/WCRP): New precision radiometry for climate research. *Bull. Amer. Meteor. Soc.*, **79**, 2115–2136, https://doi.org/10.1175/1520-0477(1998)079<2115:BSRNBW>2.0.CO;2.

Pinker, R. T., B. Zhang, and E. G. Dutton, 2005: Do satellites detect trends in surface solar radiation? *Science*, **308**, 850–854, https://doi.org/10.1126/science.1103159.

Stephens, G. L., and Coauthors, 2012: An update on Earth's energy balance in light of the latest global observations. *Nat. Geosci.*, **5**, 691–696, https://doi.org/10.1038/ngeo1580.

Takenaka, H., T. Y. Nakajima, A. Higurashi, A. Higuchi, T. Takamura, R. T. Pinker, and T. Nakajima, 2011: Estimation of solar radiation using a neural network based on radiative transfer. *J. Geophys. Res.*, **116**, D08215, https://doi.org/10.1029/2009JD013337.

Tang, W. J., J. Qin, K. Yang, F. X. Zhu, and X. Zhou, 2021: Does ERA5 outperform satellite products in estimating atmospheric downward longwave radiation at the surface? *Atmos. Res.*, **252**, 105453, https://doi.org/10.1016/j.atmosres.2021.105453.

Wang, K., and R. E. Dickinson, 2013: Global atmospheric downward longwave radiation at the surface from ground-based observations, satellite retrievals, and reanalyses. *Rev. Geophys.*, **51**, 150–185, https://doi.org/10.1002/rog.20009.

Wang, T. X., and Coauthors, 2018: Cloudy-sky land surface longwave downward radiation (LWDR) estimation by integrating MODIS and AIRS/AMSU measurements. *Remote Sens. Environ.*, **205**, 100–111, https://doi.org/10.1016/j.rse.2017.11.011.

——, J. Shi, Y. Ma, H. Letu, and X. Li, 2020: All-sky longwave downward radiation from satellite measurements: General parameterizations based on LST, column water vapor and cloud top temperature. *ISPRS J. Photogramm. Remote Sens.*, **161**, 52–60, https://doi.org/10.1016/j.isprsjprs.2020.01.011.

Wang, W. H., and S. L. Liang, 2009: Estimation of high-spatial resolution clear-sky longwave downward and net radiation over land surfaces from MODIS data. *Remote Sens. Environ.*, **113**, 745–754, https://doi.org/10.1016/j.rse.2008.12.004.

Yang, J., Z. Q. Zhang, C. Y. Wei, F. Lu, and Q. Guo, 2017: Introducing the new generation of Chinese geostationary weather satellites, *Fengyun-4. Bull. Amer. Meteor. Soc.*, **98**, 1637–1658, https://doi.org/10.1175/BAMS-D-16-0065.1.

Yang, K., T. Koike, and B. S. Ye, 2006: Improving estimation of hourly, daily, and monthly solar radiation by importing global data sets. *Agric. For. Meteor.*, **137**, 43–55, https://doi.org/10.1016/j.agrformet.2006.02.001.

Yoshida, M., M. Kikuchi, T. M. Nagao, H. Murakami, T. Nomaki, and A. Higurashi, 2018: Common retrieval of aerosol properties for imaging satellite sensors. *J. Meteor. Soc. Japan*, **96B**, 193–209, https://doi.org/10.2151/jmsj.2018-039.

Zhang, X., and Coauthors, 2019: An operational approach for generating the global land surface downward shortwave radiation product from MODIS data. *IEEE Trans. Geosci. Remote Sens*., **57**, 4636–4650, https://doi.org/10.1109/TGRS.2019.2891945.

Zhou, Y. P., and R. D. Cess, 2001: Algorithm development strategies for retrieving the downwelling longwave flux at the Earth's surface. *J. Geophys. Res.*, **106**, 12 477–12 488, https://doi.org/10.1029/2001JD900144.